Marshall Plan Scholarship

Final Report

Summarization of material mechanisms in nuclear environment

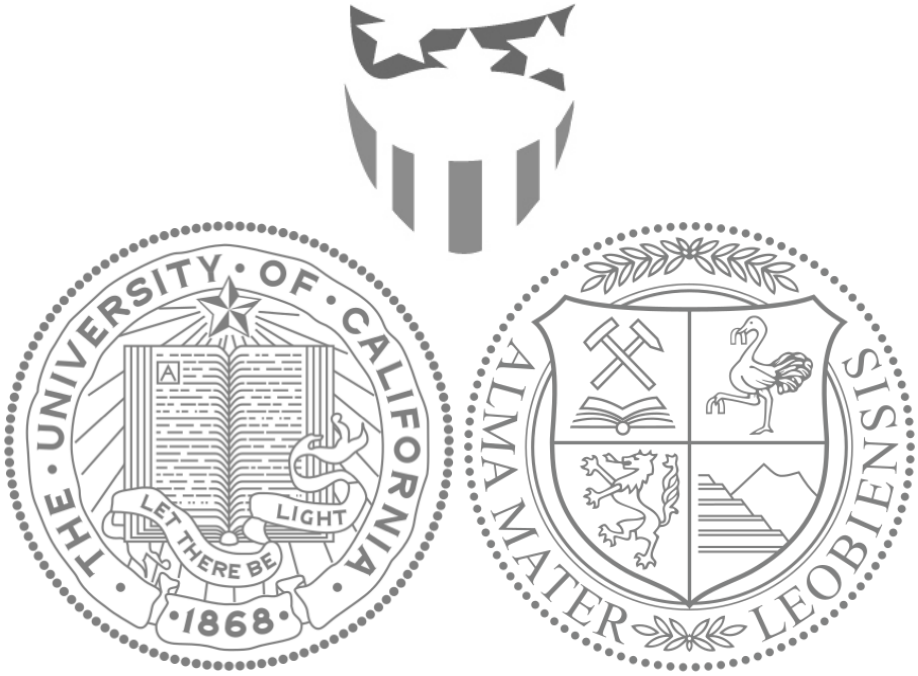

René H. Reich

Leoben, 28 January 2020

This final report documents the outcome of the research stay spent at the University of California, Berkeley – Nuclear Engineering. The report's chapters are the groundwork for the master's thesis, which will be carried out at the Montanuniversität Leoben, Department of Material Science – Chair of Design of Steels in the summer term 2020. This report is not meant for publication but the resulting master's thesis.

Table of contents

1. Introduction and problem statement

Material selection is the key step in the design process of a product. Its main objective is to choose the right material for a specific application with a specific set of tasks. These tasks vary widely, including bearing loads, conducting heat, resisting corrosion, and withstanding extreme temperatures. Because of the differences in the exposures' nature, materials are described by figures reflecting their different properties. Material property values represent experience from the past in form of former applications, measurements and material tests. They are collected for every material of interest. Thus, material selection is the step where information about the chosen material, gathered in the past, meets the predicted loads caused by the application in the future [1].

The collection of material properties is an essential aspect in material selection. The more types of materials and the more information about them are available, the better and more specific a selection one can decide. Furthermore, the quality of the collected information ensures reliability within the process. Big databases are an important medium of information collection and transportation. With their size, the amount of maintenance and support rises too. Especially the step of information gathering is a tedious job in the database creation.

The investigation of known and unknown material properties is done often in academic research often. Then, the results are published in journals, mostly online in a Portable Document Format (PDF). In 1993, Adobe Systems Incorporated developed the PDF with the goal *"to enable users to exchange and view electronic documents easily and reliably, independent of the environment in which they were created or the environment in which they are viewed or printed"* [2]. So, the PDF can be described as an electronic paper. It was never meant to transport or give access to datasets, but to represent them in a nice and readable way. The majority of scientific output from the last 40 years is distributed online by publishers in PDFs. Actually, publishers turned into a very interesting source for gathering material properties, if the datasets can be retrieved from the PDFs.

Materials in nuclear applications have to resist extreme conditions over a long time period. For example, reactor pressure vessels in nuclear power plants are designed to serve 40 to 60 years. Some of the more advanced Generation IV

reactor designs are planned to serve even 80 years. In their lifetime, they have to cope with high pressures, high temperatures, corrosive environment, and radiation damage [3]–[5].

The material well-being is crucial to the safety of the plant, its workers, and its neighborhood. Further, the fuel-cladding material performance under these harsh radiation conditions are determining the time of the fuel serving in the reactor and the power plant's efficiency consequently. Material selection for nuclear applications is therefore a step full of responsibility. On the other hand, the next nuclear reactor generation pushes to higher operating temperatures and more radiation flux, as summarized in Fig. 1. Those conditions are a challenge to the established vessel and cladding alloys. Aggravatingly, material properties for nuclear applications are provided in databases rarely, while irradiated material tests require additional attention to the examiner's safety [3]–[7].

Reactor type		Max. design temperature [°C]	Max. design pressure [MPa]	End-of-Life dose [dpa]	Reported cladding material
Generation III reactors					
Boiling Water Reactor	BWR	302	8.7	10	Zr-based alloy
Pressurized Water Reactor	PWR	351	17.7	100	Zr-based alloy
Generation IV reactors					
Supercritical Water-cooled Reactor	SCWR	550	27.5	67	Stainless steel
Very High Temperature gas-cooled Reactor	VHTR	1000	10	10	TRISO
Molten Salt Reactor	MSR	700	0.5	200	TRISO, Stainless steel
Gas-cooled Fast Reactor	GFR	850	15	200	Stainless steel
Sodium-cooled Fast Reactor	SFR	550	0.3	200	Martensitic steel
Lead-cooled Fast Reactor	LFR	500	0.1	200	Martensitic steel

Fig. 1: Operating environments and considered fuel-cladding material of Gen. IV compared to Gen. III reactors, as reported in IAEA ARIS (after [3], [4]).

This master's thesis investigates the possibilities to gather information about material properties in nuclear environments for three exemplary alloys. Fig. 1 shows that stainless steel, martensitic steel and Zr-based alloys are the most reported fuel-cladding materials. Thus, the alloys SS316, HT-9 and Zircaloly-4 are chosen as representatives for the fuel-cladding material types respectively. The data of the alloys should be retrieved from various scientific articles and papers in different journals, accessible online through the publishers Springer, Elsevier and Taylor & Francis. The gathered information should be merged to a public database and the different datasets should be computed to alloy specific materials property maps.

2. Investigated alloys

Often material selection is a compromise of competing properties. In nuclear applications, materials have to resist irradiation damage, high pressure, elevated temperatures, and corrosive environments.

Nuclear power plants use the energy from nuclear fuel. The nuclear fuel pellets have to be enclosed safely, so they can be manipulated and do not contaminate their environment. The primary task of nuclear fuel-cladding tubes is to keep the radioactive fuel pellets and their fission products enclosed safely, so they are not released in the reactor and its coolant. When in service in the power plant, the fuel-cladding material should be as transparent as possible for neutrons to minimize neutron losses. That translates to a low neutron absorption cross section of a potential material. Meanwhile, the material should have a decent service temperature to enhance the thermal efficiency of the reactor without melting. Fig. 2 shows that the material service temperature and the low neutron absorption cross section are contrary properties already [7].

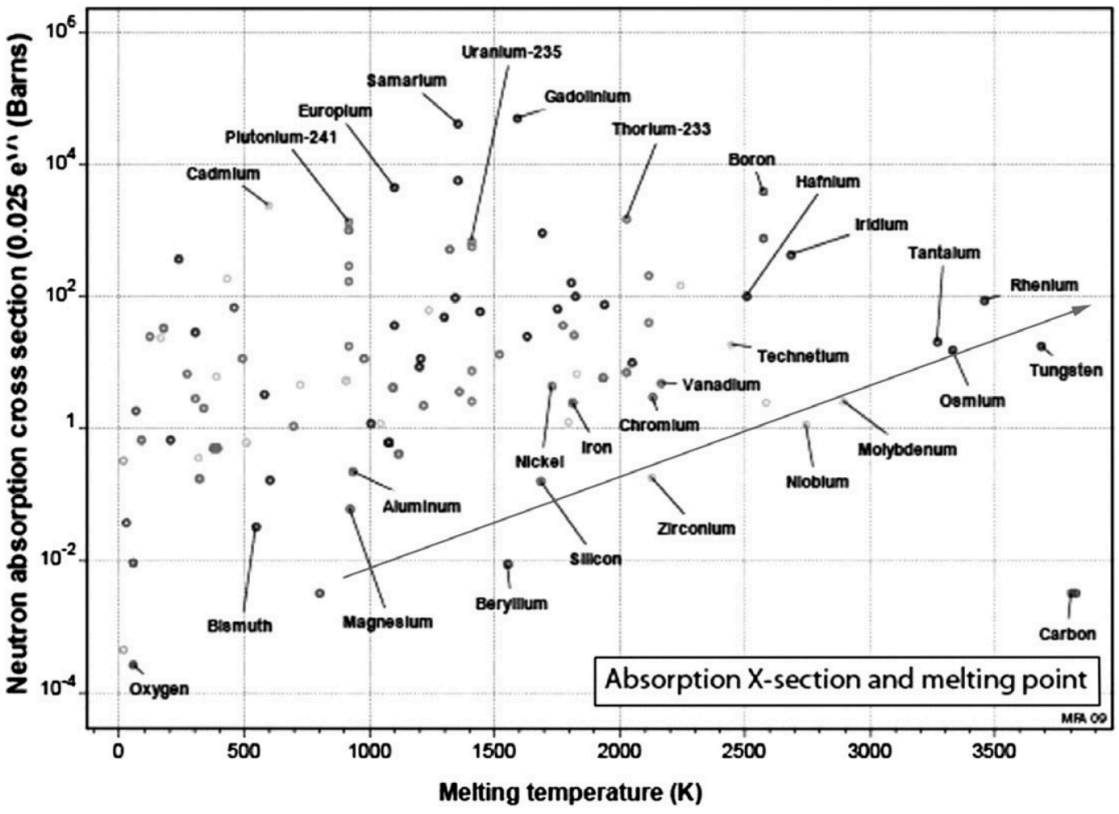

Fig. 2: Melting temperature versus neutron absorption cross section for pure elements [7].

Further, elevated service temperatures are a challenge to the material's integrity, due to creep effects. Because of the aggressive conditions inside the tube full of fuel pallets and fission products inside and the environment of the reactor's coolant and moderator on the outside, the tube material should be corrosion resistant on both sides. Most important for a thermal power plant, the fuel-cladding tube should conduct heat from the inside fuel to the coolant as efficient as possible [7].

Based on the outlined considerations, martensitic steels, austenitic stainless steels, and zirconium-base alloys are largely chosen as fuel-cladding materials. In this thesis, one alloy of each category is appointed exemplarily:

- UNS S31600, also known as EN 1.4401, X5CrNiMo17-12-2, or SAE grade 316 steel (SS316), is one of the first stainless steels developed and often used in nuclear applications.
- UNS S42100: The martensitic steel is more know under its trade name "Sandvik HT-9".
- UNS R60804: The zirconium-base alloy, called "Zircaloy-4", is the most frequent used fuel-cladding tube material in conventional commercial reactors.

The significant alloying elements of the enumerated materials are summarized in Fig. 3, according to the ASTM International specifications [8], [9].

Elements [wt. %]	**UNS S31600 "SS316"**	**UNS S42100 "HT-9"**	**UNS R60804 "Zircaloy-4"**
Carbon (C)	0.040 – 0.060	0.17 – 0.23	
Chromium (Cr)	17.0 – 18.0	11.0 – 12.5	0.07 – 0.13
Nickel (Ni)	13.0 – 14.0	0.30 – 0.80	
Molybdenum (Mo)	2.00 – 3.00	0.80 – 1.20	
Tungsten (W)		0.40 – 0.60	
Vanadium (V)	< 0.05	0.25 – 0.35	
Tin (Sn)			1.20 – 1.70
Iron (Fe)			0.18 – 0.24
Iron + Chromium			0.28 – 0.37

Fig. 3: Significant alloying elements of the investigated alloys in wt.% [8], [9].

Steel is a ferrous material with maximum 2.06 wt.% carbon. Depending on the temperature, alloying elements, and production's cooling rate, steel can exhibit different lattice structures. It can be present as face-centered cubic (fcc), called "austenite". In the case of slow cooling rates, steel can form a body-centered cubic (bcc), called "ferrite". The body-centered tetragonal structure (bct) is called "martensite", which occurs at sufficient carbon content and faster cooling rates.

In the absence of other alloying elements, the austenitic configuration in steel is present only between 1766K and 996K. One of the alloy elements that stabilizes the face-centered cubic lattice of steel down to room temperature is nickel. The high nickel content ensures that the SS316 alloy has a face-centered cubic structure at room temperature and is therefore an austenitic steel. Because of its atomic lattice, this alloy is well-malleable. The principal part of strength in austenitic alloys is based on cold-work hardening.

HT-9 is a ferritic-martensitic steel, as a result of the low nickel amount and high cooling rates in the material's heat treatment after forging and shaping. Like in a composite, the martensite contributes hard and brittle properties, while the ferrite is more ductile in the HT-9 structure. Until the 1970s, austenitic stainless steels were the primary fuel-cladding material. Ferritic-martensitic steels show higher thermal conductivity and lower expansion coefficients than austenites. Void swelling hinders the application of the high-swelling austenitic steels as cladding material. On the other hand, the bcc-bct-structure and its large amount of interphases, grants HT-9 excellent irradiation resistance to void swelling [10], [11], as shown in Chap. 3.1.

Due to the chromium content above 10.5 wt.%, SS316 and HT-9 form a thick chromium oxide passive layer that makes them corrosion-resistant in the atmosphere. The addition of molybdenum makes steels more resistant against corrosion attacks by chlorides and reducing acids.

As shown in Fig. 2, pure zirconium has an over ten times smaller neutron absorption cross section than iron. This great neutron transparency makes zirconium an interesting fuel-cladding material. Further, zirconium shows similar physical properties as iron, but is more thermal stable and corrosion resistant. Zirconium and its alloys have a hexagonal closed-packed (hcp) crystal structure. It forms willingly a stable passive layer out of zirconium oxide on its surface, which

is the reason behind the stainless property. In water, zirconium reacts to zirconium oxide under release of hydrogen gas. This exothermic reaction is quite slow at lower temperatures but speeds up exponentially with temperature increase. The formation of big amounts of hydrogen gas might lead to loss of contact between the cladding material and the reactor's coolant. Moreover, hydrogen is explosive in contact with the oxygen, e.g. form the air. In power plants, this scenario shall be avoided [12], [13].

To increase the strength and the corrosion resistance of zirconium, alloying elements are added. Tin, chromium and iron provide biggest strengthening while the neutron transparency is barely reduced. Between 200°C and 400°C, zirconium absorbs hydrogen, increasing the volume and embrittlement of the metal. Therefore, the amounts of nickel and iron in the Zircaloy have to be limited [12], [13].

All three described materials have in common that their corrosion and irradiation behavior are the limiting factors for fuel used in power plants. Their swelling, corrosion and embrittlement rates determine the service time of fuel in the reactor [14].

3. Nuclear environment

Nuclear power plants make use of thermal energy from nuclear fission reactions to generate electricity. This fission reactions are driven by a bombardment of neutrons. A neutron can interact in different ways with the core of an atom:

- When the incoming particle transfers its complete kinetic energy to the emitting particle it is called “elastic scattering”.
- When the emitted particle is the same as the captured one, but a loss of kinetic energy occurs during the particle transition, it is called “inelastic scattering”.
- Reactions where two neutrons are release after the neutron capture by the nucleus are called “$(n, 2n)$ reactions”. Because this reaction type produces additional neutrons, it is essential to keep the chain reaction in the reactor core running.
- Nuclear reactions where a photon (γ), a proton (p), or an alpha particle (α) is emitted are called (n, γ), (n, p), or (n, α) reactions respectively.

Based on their kinetic energy, the two most important classes of neutrons are the fast neutrons (E > 1 MeV) and the slower thermal neutrons (E = 0.025 eV). The neutron energy influences how and with which atom the neutron will interact [15]. Although thermal reactors have a mixed neutron spectrum with a wide range of neutron energies, they slow many neutrons down to thermal neutrons for the upkeep of the nuclear chain reaction. Fast reactors, also called “breeders”, sustain their chain reaction by fast neutrons. Nowadays, most of the nuclear power plants have thermal reactors, but half of the for the future proposed Generation IV reactors are fast reactors [5].

So far, just metal alloys are used for reactor pressure vessels and fuel cladding materials. Hence, the interactions of neutron radiation with metals are of special interest. The neutron, as an energetic projectile, strikes one or several atoms in the vessel or cladding material. If the energy of the incoming neutron is high enough, the interaction can lead to the displacement of the target atom from its lattice site. The vacant site left behind is called “vacancy”. The displaced atom could interact with other atoms, find another vacancy to occupy, or embed itself between regular occupied lattice sites. Atoms embedded between lattice sites are called “interstitial” atoms. The pair of a vacancy and an interstitial atom is

called “Frenkel Pair” and it is the primary cause for physical and mechanical changes of the irradiated metal [15].

To describe the atomic damage within an alloy, the unit “displacements per atom” (dpa) established in radiation material science. It quantifies the number of displacements every atom went through statistically. The unit depends on the radiation flux ϕ, the displacement cross section σ_D, the time the material was irradiated t, and the maximum and minimum radiation energies E_{max}, E_{min}:

$$dpa = \int_{E_{min}}^{E_{max}} \phi(E) \cdot \sigma_D(E) \cdot t \cdot dE. \qquad \text{(Eq. 1)}$$

The displacement cross section σ_D is an intrinsic property of the irradiated material at a certain incoming radiation energy. It indicates how much energy is transferred from the particle to the atom at the collision and how many displacements the knocked-out atom will cause. It is important to emphasize that dpa has no linear correlation with the radiation fluence, because dpa includes a material characteristic. More general, the unit can be described as a ratio:

$$dpa = \frac{R}{N} \cdot t, \qquad \text{(Eq. 2)}$$

where R is the the number of displacements per unit volume per unit time, t is the irradiation time, and N is the atom number density [15].

These ongoing displacements and the accompanied Frenkel Pairs result in physical changes of the material, such as swelling, growth, phase change, and segregation. Moreover, irradiation varies the mechanical properties such that materials perform much differently than their unirradiated equivalents. Some examples of mechanical effects due to irradiation are swelling, hardening, embrittlement, loss of creep strength, accelerated corrosion, and intergranular cracking [15]. The following chapters describe some of these mechanical effects in more detail.

3.1. Irradiation swelling

Swelling is a dimensional instability and it describes a change of the linear dimensions whereas the volume of the component increases too. This imposes a challenge to reactor engineers and designers. The volume change is caused by the formation and growth of voids and bubbles within the material. Bubbles are cavities filled with insoluble gas, which provides internal pressure that stabilize the cavity. Voids are empty cavities only stable under a flux of vacancies. So, voids are formed by precipitation of irradiation-induced vacancies [16]. Swelling can be measured by the volume change ΔV compared to the initial volume V:

$$\frac{\Delta V}{V} = \frac{4\pi}{3} \int_0^\infty R^3 \cdot \rho_V(R)\, dR, \qquad \text{(Eq. 3)}$$

where $\rho_V(R)\, dR$ is the number of voids per volume with radii between R and $R + dR$. When the radius distribution is narrow, the integral can be simplified to:

$$\frac{\Delta V}{V} = \frac{4\pi}{3} \cdot \bar{R}^3 \cdot \rho_V, \qquad \text{(Eq. 4)}$$

where $\bar{R}$ is the mean void radius [15]. Normally, the volume change $\frac{\Delta V}{V}$ is represented in percent.

While the fast-moving interstitial atoms tend to migrate until the verge of the cascade, the slower-moving vacancies tend to form clusters nearby. So, vacancies need some mobility to cease as a void [16]. Brimhall et al. [17] showed that at low temperatures the low defect mobility hinders void growth. High temperatures and the thermal motion of the atoms lead to vacancy annihilations, as described in Chap. 4. These two void destructive mechanisms result in a peak at intermediate temperature, as shown in Fig. 4. So, the lower temperature limit for void formation is commonly set around 300°C [18]–[20].

Garner and Gelles [21] describe a steady-state swelling rate in austenitic stainless steels around 1 %/dpa over a wide dose range between 427°C and 650°C. Fig. 5 displays that an onset dose is needed to start void swelling and that just the incubation dose, which lays in between the onset dose and the steady-state swelling, increases with lower irradiation temperature.

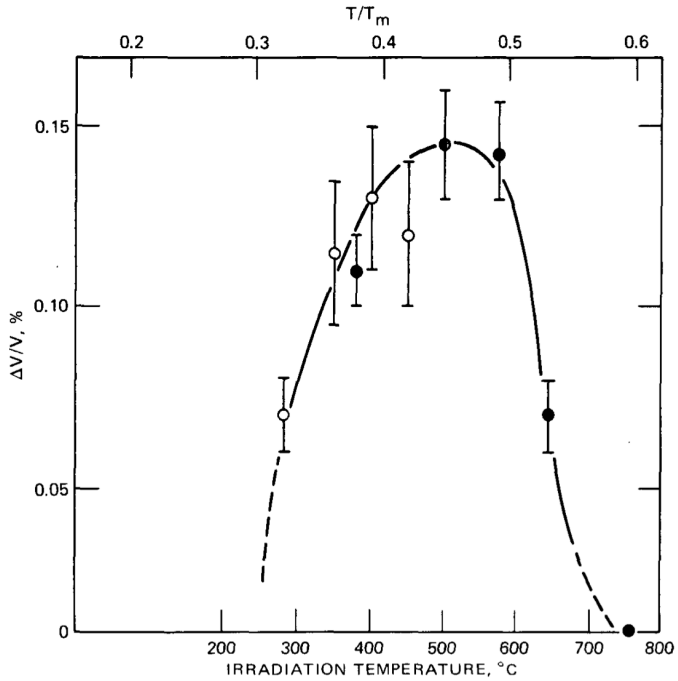

Fig. 4: Swelling (in %) in pure nickel depending of the irradiation temperature at a constant neutron fluence [17].

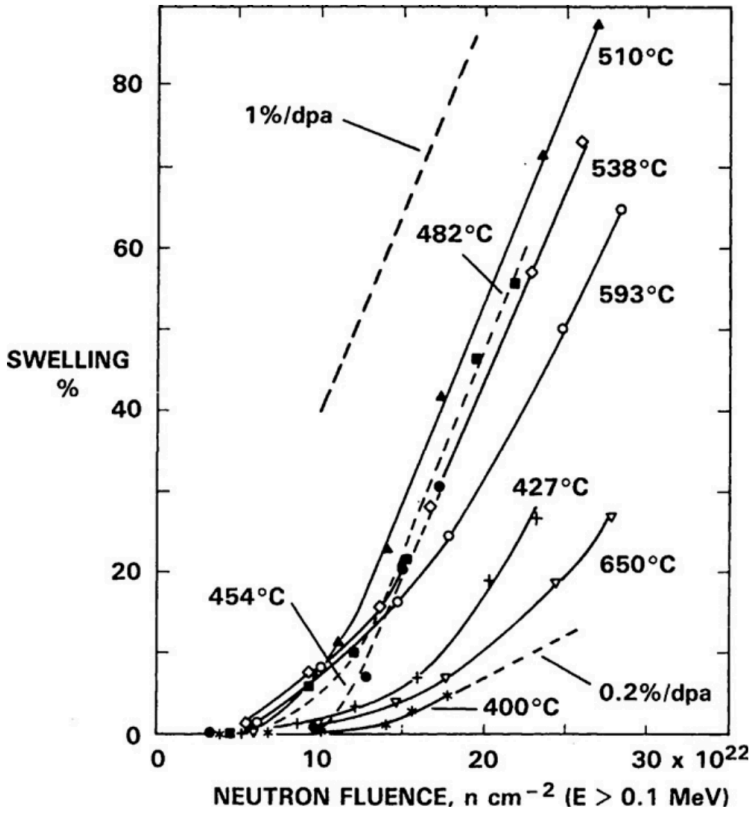

Fig. 5: Swelling as a function of neutron fluence and irradiation temperature for 20% cold-worked SS316 [21].

Alloy elements can affect the material's irradiation swelling behavior. In Fe-Cr-Ni austenitic alloy, swelling drops with increasing nickel content and increases with rising chromium content. Minor elements can reduce the mobility of either vacancies or interstitials by binding them with sufficient strength. Precipitates can delay void growth or initiate vacancy-interstitial annihilation. Induced stress, e.g. by cold work, reduces the transient swelling period before reaching the steady-state rate. Fig. 6 shows schematically the difference in swelling behavior between SS316 and ferrites. Just considering swelling, the figure also indicates the advantage of the ferritic-martensitic HT-9 alloy over SS316 as fuel-cladding material [10], [15], [22].

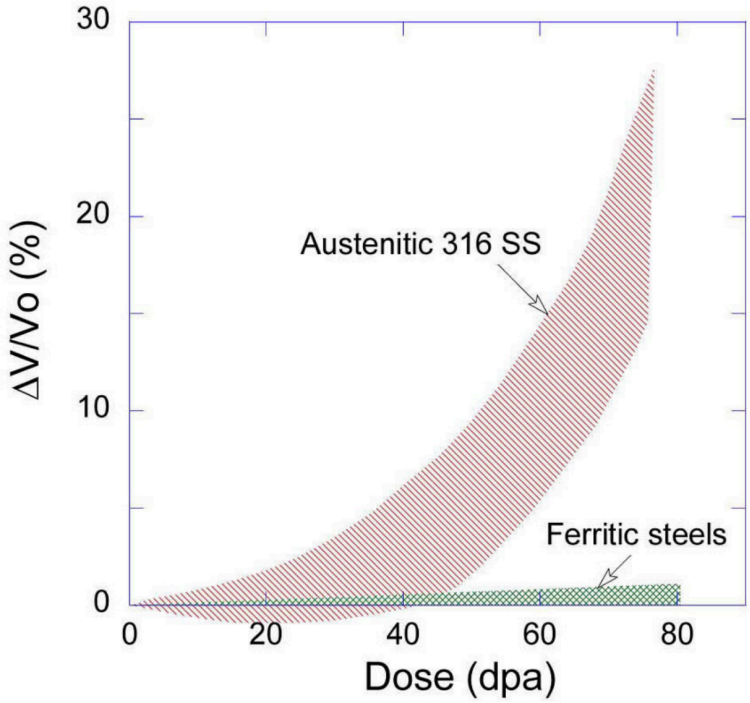

Fig. 6: Schematic swelling behavior of SS316 and ferritic steels [22].

The mechanics of voids and bubbles in the material are distinct. Beside the volumetric change, gas bubbles modify the material's physical and mechanical properties substantially. A major source for bubbles is the helium production within the alloy. Induced by thermal neutrons, boron and nickel decay emitting an alpha particle:

$$^{10}B(n,\alpha)\ ^{7}Li, \qquad \text{(Eq. 5)}$$

$$^{58}Ni(n,\gamma)^{59}Ni(n,\alpha)^{56}Fe. \qquad \text{(Eq. 6)}$$

Despite the higher dose, material's helium swelling is lower in fast reactors than in thermal reactors. It is possible that hydrogen is generated in alloys in the same manner, but through different reactions. Also, corrosion and decomposition of cooling water can diffuse hydrogen, which accumulates in the material's cavities [15], [23].

3.2. Irradiation hardening

The formation and mobility of dislocations determine the plasticity of a material. Thus, two types of hardening can be described [15]:

- Source hardening is the increase in unpinning stress, required to unlock a dislocation from its source and set it in motion.
- Friction hardening is the increase of flow stress, which a dislocation needs to stay in motion.

Irradiation can produce defect clusters close to Frank-Read sources. These clusters hinder the expansion of loops. Once the stress level is high enough for the loop to destroy the cluster, the dislocation can be released. So, irradiation can increase source hardening [15].

The motion of a dislocation can be hindered by obstacles in its slip plane or by other dislocations and their stress fields. Examples for obstacles are defect clusters, loops, precipitates, bubbles or voids and their interaction with dislocations is called "short-range stress". The interaction of dislocations with each other or with dislocation networks is called "long-range stress" [15]. Fig. 7 shows the increasing network dislocation density over the dose in austenitic steels. The true contribution of the different hardening mechanisms is not fully understood yet, but Lucas [24] predicted the different proportions to yield stress increase of austenitic stainless steel, as shown in Fig. 8.

From Fig. 7, saturation of irradiation hardening can be derived, when the creation and the destruction of obstacles equilibrate by irradiation damage, other dislocations, or temperature. Taking this into account, the yield stress increment due to irradiation hardening can be described by an exponential formula:

$$\Delta\sigma_y = A \cdot [1 - \exp(-B \cdot \phi \cdot t)]^n, \qquad \text{(Eq. 7)}$$

where is ϕ the radiation flux, t is the irradiation time, n is an exponent to fit the model, and A and B are material specific parameters depending on the temperature [15].

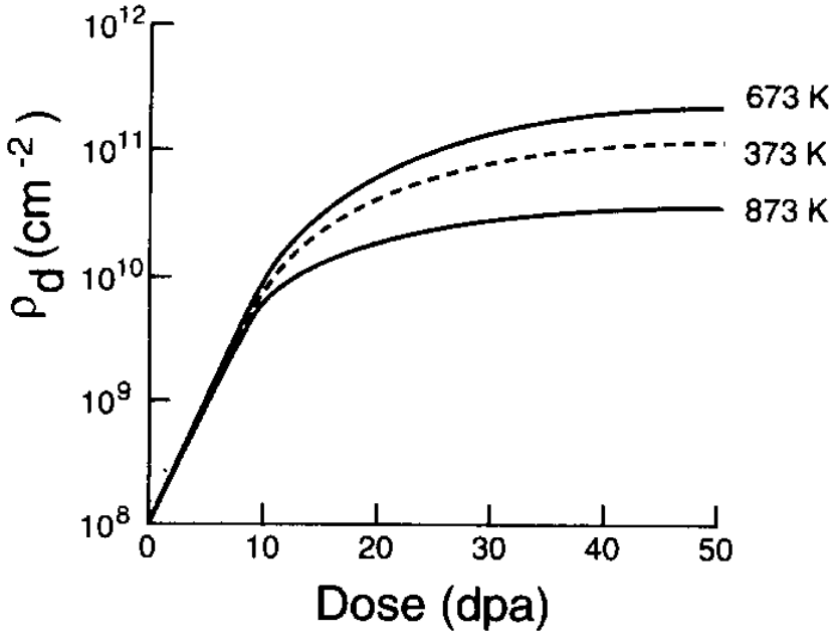

Fig. 7: Network dislocation density ρ_d at different dose and irradiation temperature [15].

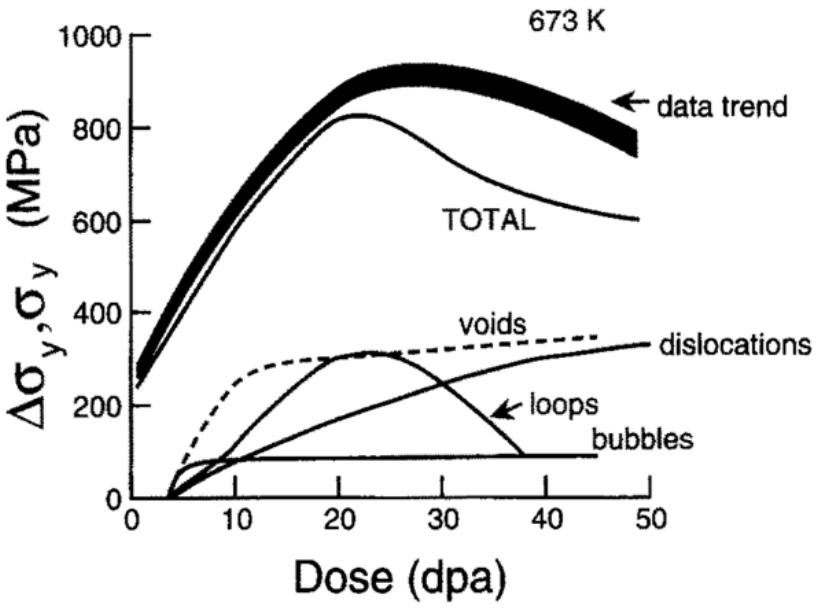

Fig. 8: Model predictions of the various contributions to yield stress change at 673K [24].

Thus, irradiation hardening can be described by the increment of the metal's mechanical properties, like yield strength or ultimate tensile strength. Normally, this material behavior is investigated in a tensile test. In a tensile test a metal specimen is loaded with a uniaxial tensile force, while the material's elongation and the tensile force are recorded. The output can be plotted in a stress-strain curve. Fig. 9 shows two schematic stress-strain curves for fcc (a) and bcc (b) metals and the effect of irradiation with increasing dose [15].

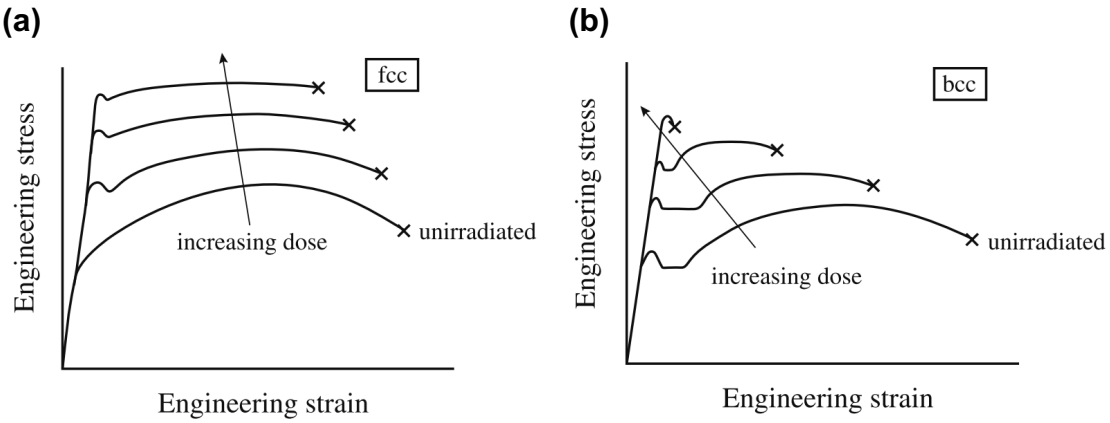

Fig. 9: Schematic stress-strain curves for fcc **(a)** and bcc **(b)** metals and the effect of irradiation with increasing dose [15].

Alternatively, hardness can be defined as the material's resistance against deformation. Hence, hardening is an increase of that resistance. Material tests, following that principle, are based on a well-defined and harder specimen intruding the material's surface. A well-known example of such a test is the Vickers hardness test, where a standardized, pyramid shaped diamond is used to indent the test probe by a standardized amount of load. The diagonals of the remaining indentation in the material are then computed to the so-called Vickers hardness number (HV). The higher the material's hardness, the smaller is the indentation, the higher is the HV number. Based on empirical data, Busby et al. [25] showed that yield strength and Vickers hardness are related with each other in austenitic and ferritic steels.

3.3. Irradiation embrittlement and fracture

Embrittlement is the material's loss of resistance to cracking by decreasing plastic and creep deformation before fracture. Although, the transition is smooth and arbitrary, two extreme types of fracture can be distinguished:

- Ductile fracture shows significant plastic deformation prior and during the crack propagation.
- Brittle fracture exhibits no gross deformation, very little microdeformation, and fast crack growth rates.

Further, fractures can be classified by the path they take through a polycrystalline material:

- Trans-granular cracks propagate through the grains.
- Inter-granular cracks propagate along the grain boundaries between the grains.

Depending on the alloy, temperature, state of stress, and loading rate, metals can show all these types of fracture [15].

Depending on the force propagating the crack, three basic modes of fracture can be defined, as depicted in Fig. 10:

(a) Mode I describes a tensile load normal to the crack plane opening the crack.
(b) In Mode II the load shears the surfaces in plane, normal to the crack front.
(c) In Mode III the load shears the surfaces out of plane, parallel to the crack front.

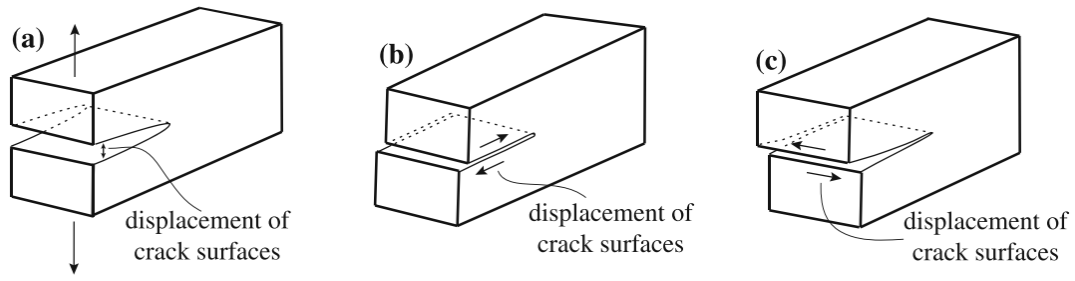

Fig. 10: The three basic fracture modes: Mode I **(a)**, Mode II **(b)** and Mode III **(c)** [15].

In practice, Mode I is the harshest to the material and it is therefore the most examined one [15].

The stress big enough to advance the fracture is called fracture stress σ_f. Actually, the crack gets propagated based on the stress field around its tip. So, to define a stress intensity factor comes handy. Especially, the critical stress intensity where the crack propagation turns into an overload fracture is essential. Based on the work of Griffith, Irwin [26] found that the critical stress intensity for a crack with a length of $2a$ in an infinite plane, which is uniform uniaxial loaded (Mode I), can be defined as:

$$K_{Ic} = \sigma_f \cdot \sqrt{\pi \cdot a}, \qquad \text{(Eq. 8)}$$

where K_{Ic} is also called fracture toughness. Infinite plates are hard to realize in materials test. So, normally a geometry correction coefficient is multiplied to (Eq. 8.

The fracture toughness K_{Ic} assumes that the stress states do not change at the tip of the crack. So, loads above K_{Ic} lead to brittle fracture immediately. Indeed, ceramics and steel at low temperatures show such a behavior. This linear-elastic fracture mechanics is valid at high yield strength and the component thickness is big. However, most steel alloys behave described by elastic-plastic fracture mechanics, which also considers plastic hardening around the crack tip. To convert the geometry dependent fracture toughness to a geometry independent material characteristic for elastic-plastic behavior, Cherepanov [27] and Rice [28] suggested the so-called J-integral:

$$J = \int_{\Gamma} W\, dy - T\left(\frac{\partial u}{\partial x}\right) ds, \qquad \text{(Eq. 9)}$$

where Γ is a counterclockwise contour around the crack tip, W is the strain energy density, T is the traction vector normal to an element ds, and u is the displacement vector, as shown in Fig. 11.

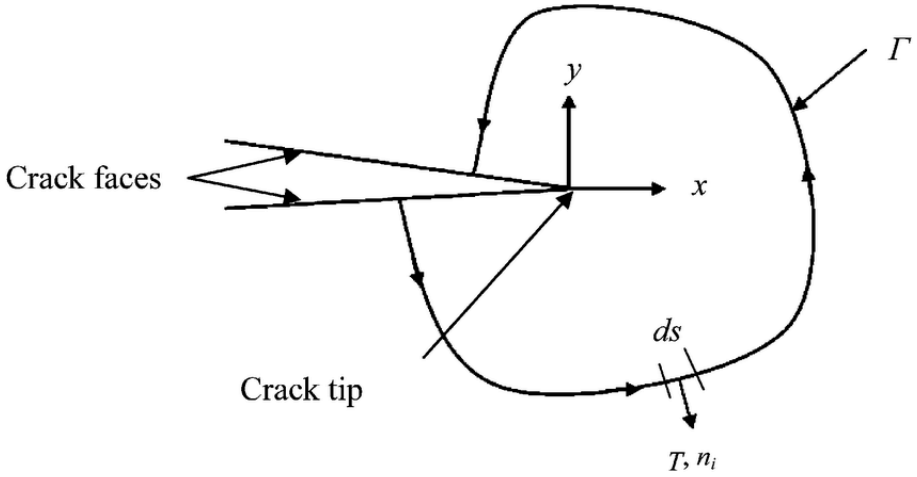

Fig. 11: Definition of the J-integral at the crack tip with the counterclockwise contour Γ and the traction vector T, normal to an element ds [28].

Physically spoken, the J-integral quantifies the difference in potential energy of two equivalent specimens having slightly different crack lengths. For elastic-plastic strain conditions its correlation to the fracture toughness is:

$$J_{Ic} = \frac{1-\nu^2}{E} \cdot {K_{Ic}}^2, \qquad \text{(Eq. 10)}$$

where ν is the Poisson's ratio and E is the elastic modulus [15].

The ASTM International standard E399 describes two sample designs to measure K_{Ic}: the 3-point loaded notched beam and the compact tension specimen. Because the fracture toughness measurements rely on the validity of linear-elastic fracture mechanics, the specimens' dimensions have to be regulated [29].

Particularly, in nuclear applications a sudden brakeage of a material could expose humans and the environment to danger. Thus, nuclear power plants follow the leak-before-brake concept [30]. It describes that a slowly ductile failing part forming a leak and warning the staff thereby is preferable to an immediate, catastrophic breaking of the part. Accordingly, the transition from material's brittle to ductile behavior is of peculiar interest. Therefore, a notched bar impact test, also called Charpy impact test, is performed [31]. In a Charpy impact test a pendulum swings through a notched bar made out of the investigated material. In the impact moment of the pendulum's hammer in the bar, some kinetic energy is transferred to break the specimen. Because the weight of the pendulum is

known, the height difference between the test start and after the impact quantifies the energy needed to break the material. As the geometry of the bar and the notch effect the fracture energy result, they have to be standardized.

The Charpy test can be repeated with various heated or cooled bars of the same alloy. The obtained impact energies can be plotted depending on the specimens' temperatures in a Charpy impact curve, as shown in Fig. 12.

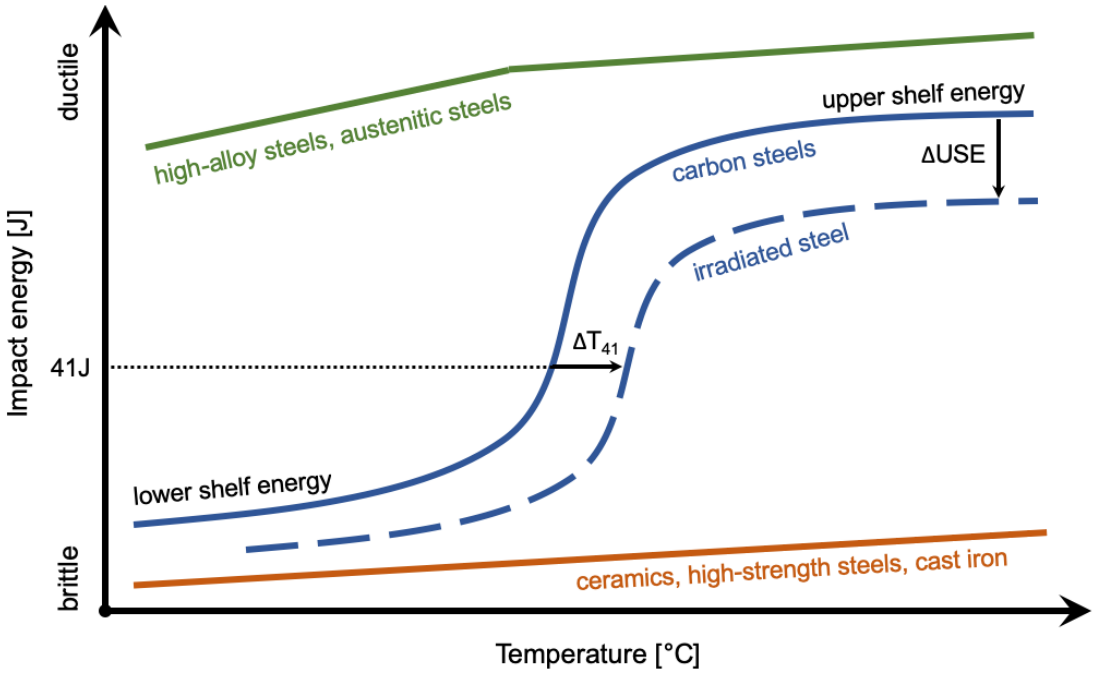

Fig. 12: Schematic Charpy curves for different materials and effect of irradiation on the Charpy curve of carbon steels.

Fig. 12 depicts the schematic Charpy curves for various types of materials. With increasing temperature, the carbon steel Charpy curve shows the transition from brittle behavior, called lower shelf energy, to ductile behavior, called upper shelf energy. Because the brittle-ductile transition is smooth, the transition temperature has to be defined by standardized aspects. It is common to define the transition temperature at a fixed impact energy level, for example the transition temperature at 41J of impact energy (T_{41}). The ASME BPVC III [31] and NRC 10 CFR part 50 define a reference temperature of nil-ductility (RT_{NDT}), at which the specimens initiate the fracture without any plastic deformation. Based on the Charpy impact test results, the RT_{NDT} is defined by a minimum impact energy and by a minimum of lateral expansion of the fractured specimens. Further, a ductile-to-brittle transition temperature (DBTT) can be defined as the intersection point of the

fracture stress curve and the yield stress curve over the temperature, as shown in Fig. 13 (a) [15].

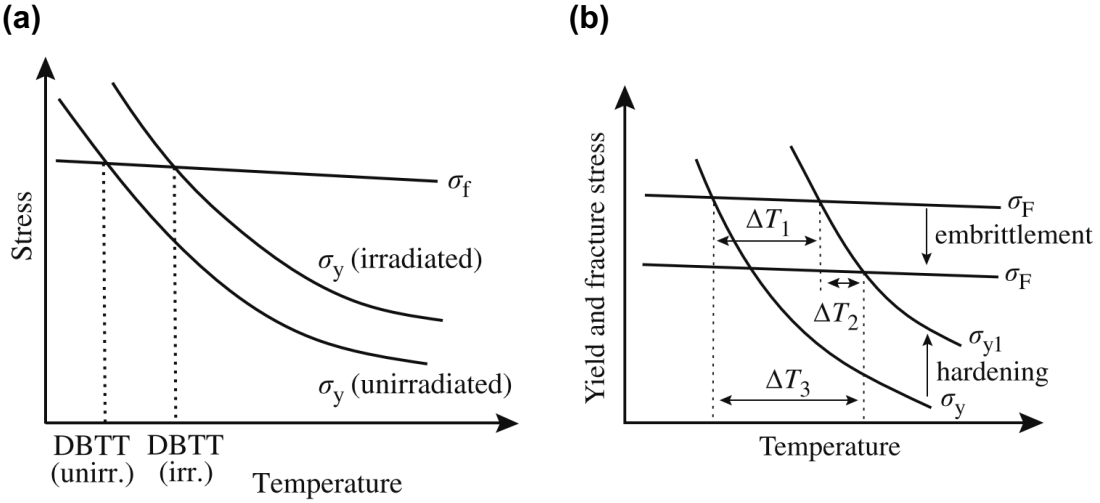

Fig. 13: Schematic fracture stress σ_f and yield stress σ_y curves showing the ductile-to-brittle transition temperature (DBTT) **(a)** and the effect of irradiation on the DBTT **(b)** [16], [23].

The neutron environment, the exposure temperature, the steel composition, and the steel microstructure affect the degree of embrittlement. The schematic Charpy curve in Fig. 12 indicates the effect of irradiation. Obviously, the irradiation damage decreases the upper shelf energy by a so-called upper shelf energy shift (ΔUSE) and the transition temperature is shifted by ΔT_{41}. Irradiation can cause the formation of precipitates or the segregation of trace elements in the alloy, which both lead to a decrease of the fracture strength. Together with the yield strength increment by irradiation hardening, as described in Chap. 3.2., Fig. 13 (b) explains the transition temperature shift to higher values, e.g. for DBTT.

As mentioned at the end of Chap. 3.1, hydrogen can possibly enter an alloy by corrosion, diffusion, or nuclear reactions. Beside swelling, hydrogen causes embrittlement, additionally to the direct irradiation effects. There are several theories trying to explain how hydrogen does that, reaching from the weakening of the metal-metal bonds till the formation of stress increasing bubbles. In zirconium, hydrogen forms the brittle hydride ZrH_2. Thus, hydrogen embrittlement is a crucial mechanism in ferritic steels, nickel-base and zirconium-base alloys [15].

3.4. Irradiation creep

Creep is a time-dependent dimensional instability, like swelling, but it describes a change of linear dimension at a constant volume of the component. Without irradiation effects, creep occurs under constant load just at high temperatures in metals. At temperatures lower than 30% of the alloy's melting point ($T/T_M < 0.3$), creep can normally be neglected.

Depending on the stress and the temperature, creep is caused by two major deformation mechanisms. Ashby [32] suggested to summarize the different mechanisms in a single plot, called "deformation mechanism map". Fig. 14 is the very first published deformation map by Ashby.

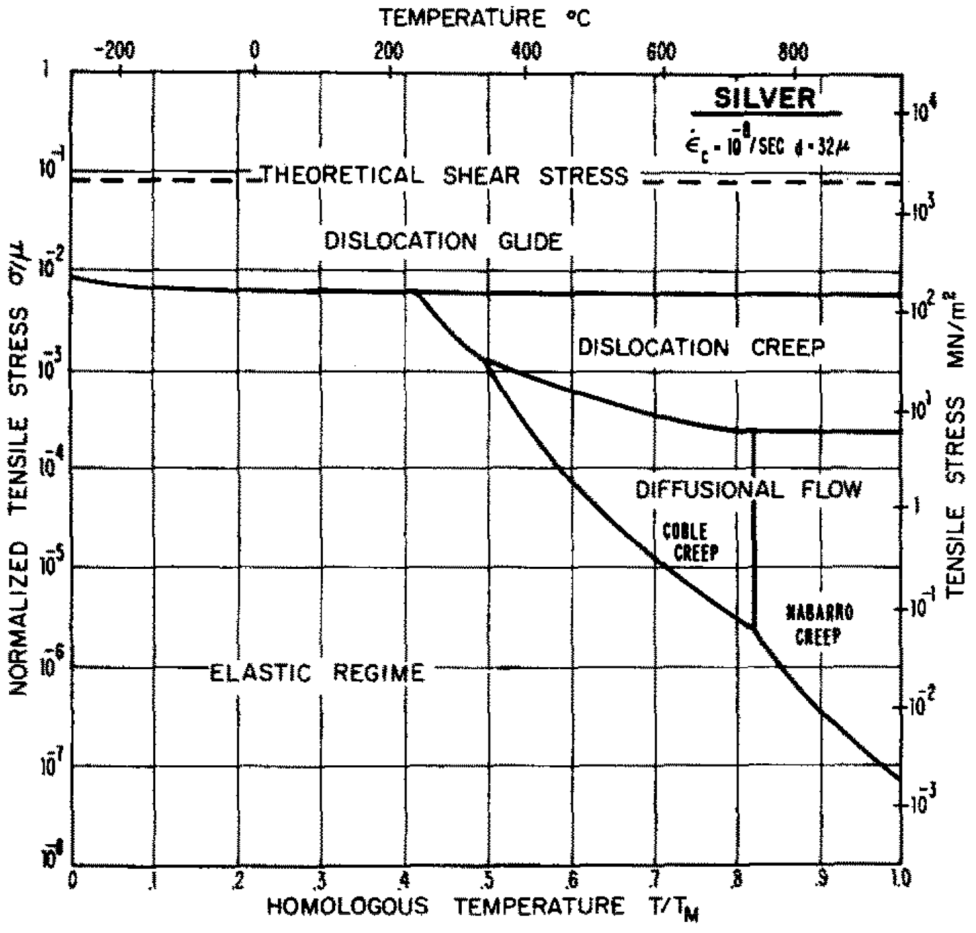

Fig. 14: The very first published deformation-mechanism map by Ashby. It is the map for pure silver of grain size 32 μm and a critical strain rate $\dot{\varepsilon}_c$ rate of 10^{-8} s^{-1} [32].

Fig. 14 illustrates that creep is the time, temperature and stress-dependent component of plastic strain, indicated as “dislocation glide” in the map. At temperatures just above 200°C, the field of dislocation creep emerges. Due to the high temperatures, dislocations have enough energy to climb hindering obstacles like the ones explained in Chap. 3.2. The gliding of the so freed dislocation causes the dimensional changes. Diffusional creep, indicated as “diffusional flow” in Fig. 14, describes the migration of atoms in the one and vacancies in the opposite directions resulting in dimensional changes. The subfields “Coble creep” and “Nabarro-Herring creep” just indicate grain-boundary or bulk diffusion respectively as prevalent atom and vacancy diffusion mechanism [15], [32].

Compared to the thermal creep described so far, irradiation widens the creep domains to lower temperatures and increases the creep rate compared to thermal creep at the same temperature. As discussed in the previous chapters, irradiation influences the actions of dislocation. Thus, irradiation impacts diffusional creep. Generally, the deformation caused by irradiation creep can be described as:

$$\varepsilon = \frac{\Delta l}{l_0} = A \cdot \left[1 - exp\left(-\frac{\phi \cdot t}{C}\right)\right] \cdot \sigma + B_0 \cdot \sigma^n \cdot \phi^m \cdot t, \qquad \text{(Eq. 11)}$$

where l_0 is the initial dimension, Δl is the dimension change, ϕ is the neutron flux, t is the irradiation time, σ is the stress. The deformation ε is called tensile strain or creep strain and is described dimensionless or as percent [15].

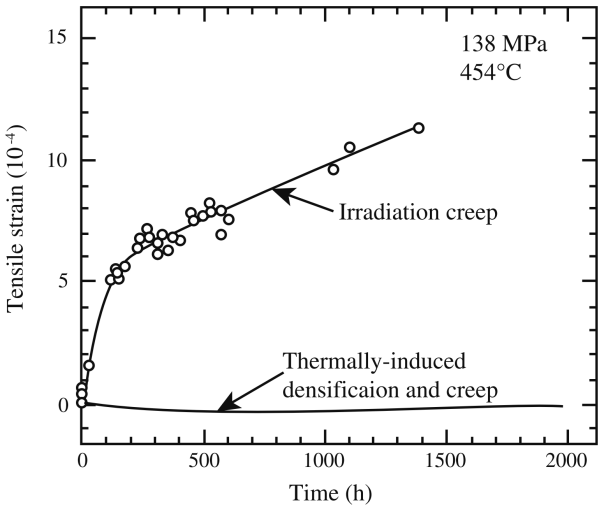

Fig. 15: Irradiation creep in 20% cold-worked SS316 loaded with 138 MPa at 454°C [15].

Similarly to swelling, irradiation creep exhibits a transient regime, described by the first term in (Eq. 11), and a steady-state regime, described by the second term. Usually, the creep strain rate depending on time ε' is of interest, but irradiation creep is often reported as effective strain rate per dpa $\dot{\varepsilon}_{eff}$ divided unit of effective stress σ_{eff}:

$$\frac{\dot{\varepsilon}_{eff}}{\sigma_{eff}} = B_0, \qquad \text{(Eq. 12)}$$

where B_0 is called “creep compliance”. If void swelling is considered too, (Eq. 12 can extended to the following empirical equation:

$$\frac{\dot{\varepsilon}_{eff}}{\sigma_{eff}} = B_0 + D \cdot \dot{S}, \qquad \text{(Eq. 13)}$$

where $\dot{S}$ is the instantaneous volumetric swelling rate per dpa and D is the creep-swelling coupling coefficient [15]. The irradiation creep mechanism can be added to Ashby’s deformation mechanism map, as shown for SS316 in Fig. 16 [33].

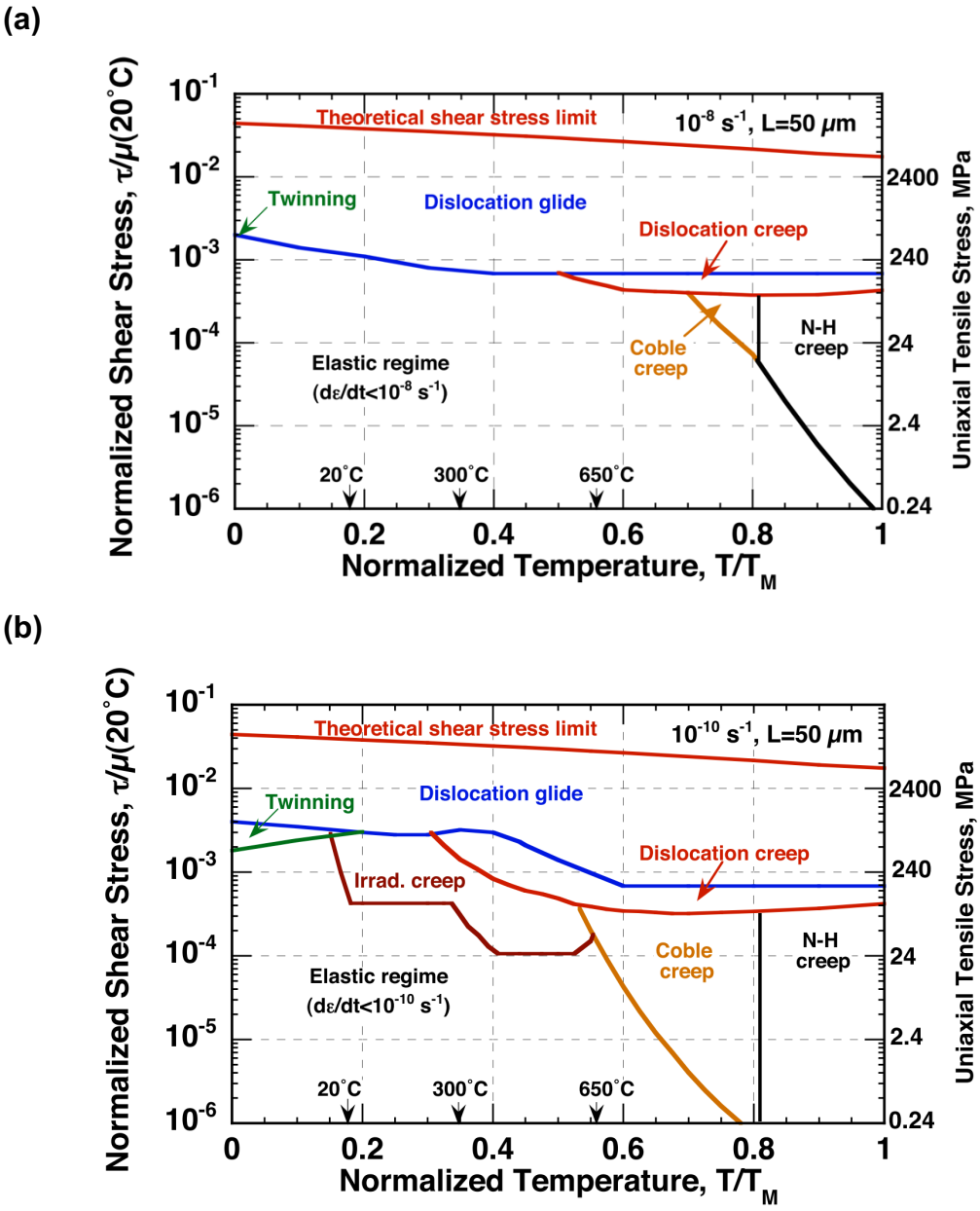

Fig. 16: Constructed deformation mechanism maps for SS316 considering just thermal creep **(a)** and extended by irradiation creep mechanism **(b)** [33].

4. Elevated temperature environment

The principal part of strength in austenitic alloys, like SS316, and in zirconium-based alloys, like Zircaloy-4, is caused by what is called work hardening. Plastic shaping of the material, e.g. bending or rolling, initiates new defects and dislocations in the crystal. In the case of sufficient number of dislocations generated, they hinder each other mutually in their movement so that a strength improvement shall occur.

With increasing temperature, the atom vibrations and movement in the steel's crystal lattice increases too. Above temperatures of 30% of the melting point ($T/T_M > 0.3$), there is enough energy to heal point defects, like interstitials and vacancies, and anneal dislocations. This processes in the material are resumed as "recovery", which results in a decrease of hardness and yield strength and in an increase of ductility. The enhanced atomic mobility causes grain growth, especially if the materials are exposed to even higher temperatures over a long period. According to the Hall-Petch equation [15], an increasing grain size lowers the material strength.

Ferritic-martensitic alloys, like HT-9, are produced by quenching, starting from temperatures where the steel is still austenitic. Due to the rapid cooling rates, the austenite forms the metastable martensite (bct) structure. The alloy's primary source of strength are the brittle martensite grains. These alloys also exhibit recovery, but more crucial are temperatures above the austenitic transformation temperature (approx. 700°C). Then, the ferritic-martensitic structure recrystallizes causing the material's loss of hardness and strength by the martensite.

In alloys with high carbon content, chromium carbide precipitates above temperatures of 500°C. These carbides impoverish the surrounding areas that then shall have no passivation corrosion protection due to local lack of chromium. Moreover, the formed carbide precipitations lead to an undesired embrittlement of the material.

5. Materials informatics

Materials informatics is a research field combining practices of informatics, data science, material science and engineering to improve the discovery, development, selection, production, use and recycling of materials. It analyses complex, multiscale information about material production, physical or chemical properties, measured and collected before. Material informatics can also be used to generate and manage material data, beside its utilization. The material informatics' objective is to compute statistically robust, physically and chemical meaningful models to enhance one or more episodes in the material's life cycle [34]–[37].

While developing a new consumer product takes two to five years, implementing new materials may take 15 to 20 years from invention till commercial launch [38]. Modern fabrication methods, like Additive Manufacturing, enable new degrees of freedom and rocketing speed of customization. These manufacturing opportunities equal challenges for traditional material science approaches to determine material process and performance limits [37], [39]. In 2011, the U.S. government introduced a multi-agency initiative, called "Materials Genome Initiative" (MGI). According to the 2014 MGI Strategic Plan, three of the four MGI's key challenges are within the materials informatics field [39].

One of the earliest examples of materials informatics are thermodynamic databases. Along the elements of the periodic table, data about the thermodynamic contribution of every element were collected. Such databases were the fundament of thermochemical computations to map phase stabilities in binary and ternary alloys. As a result, computationally derived phase diagrams are well established in material development nowadays. Another example of well-known databases in material science are crystallographic databases, like the Inorganic Chemistry Structural Database (ICSD), or the Cambridge Structural Database (CSD) [34], [36]. It is striking that mainly digital database with chemical information on an atomic level developed. Especially on the level of commercial materials and alloys, databases about corrosion behavior, processing properties, physical and mechanical properties, like yield strength or uniform elongation, are missing or just emerging [36], [37].

Materials informatics can fulfill several tasks in different steps of the material's life cycle. Rickman et al. [36] enumerates in detail a couple of application examples reaching from material discovery, ab initio calculations, multimodal imaging, phase characterization, material optimization, till application of density-functional theory.

New material development is time-consuming, risky and expansive and not every new application needs a new material. For example, the superalloy "Inconel 625" was originally developed as a structural material for supercritical steam power plants. It is famous for its high strength and corrosion resistance in highly acidic environments. However, the alloy found use in battery contacts of the Tesla Model S, due to its good stress response at extreme temperatures resulting from resistive heating of the contact at rapid acceleration [37], [40]. With more and more alloys invented, the range of available materials becomes unimaginable. So, selecting an optimal solution for a specific application turns tedious. Mulholland and Paradiso [37] explain how material informatics can be used for material selection. Based on the application's requirements and loads, machine learning tools can find an optimal candidate out of a material database.

The following three subchapters describe general concepts and methods originating outside the field of materials informatics but become essential therein.

5.1. Machine Learning

In standard programming, one defines operating instructions step-by-step resulting in an algorithm solving a specific problem. In machine learning (ML), the computer uses a set of statistical models to compute its own algorithm based on the data provided. Machine learning is a branch of artificial intelligence. It "learns" from situations from the past to estimate a model, which can fulfill different types of tasks, like classification, regression, or clustering [41].

In general, every machine learning process undergoes the following three iterative steps [41], as summarized in Fig. 17:

(1) **Representation**: First, the task's object or instance needs to be described, so the computer can understand it. The instance's attribute together with its value are called "features", e.g. "pixels = 1200", "diameter

= 15.8”, or “yield strength = 230”. In the representation step, one has to choose which and how many features to include. Further, it has to be decided which mathematical model fits best for the task. Then the ML model can be computed based on the input features. The input data teaching the ML model is called “training data”.

(2) **Evaluation**: In this step, one has to define what criterion distinguishes a good from a bad ML model.

(3) **Optimization**: Which changes will improve the model’s criterion? This question might be answered by changing the number of features, the mathematical model or its parameters.

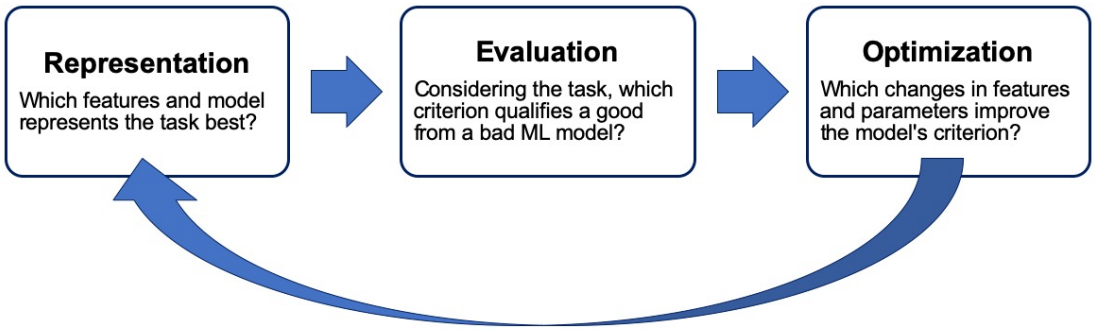

Fig. 17: Basic ML model development steps.

With the increasing number of tasks, many different systems of machine learning developed. So, it is useful to classify them in broad categories by different aspects. Just considering whether the ML model sees human supervision during its training, there are four major categories [41], [42]:

- **Supervised learning**: In supervised learning, the input data already includes the desired output, called “label” or “target”. A typical example therefor is an email spam filter where the user tells the program which emails are spam or not and the filter classifies the new incoming emails then.
- **Unsupervised learning**: As the exact opposite of supervised learning, the input data is missing information about the output totally. This might be used to detect clusters of voids in a material or to detect anomalies.
- **Semi-supervised learning**: Because labeling is often time-consuming and costly, semi-supervised learning lays between the two categories above, where just some instances are labeled.
- **Reinforcement learning**: The ML model perceives the environment to select and perform an action then. Based on the action, the ML model gets

rewards or penalties in return and it tries to find the best strategy to maximize the rewards. Reinforcement learning is often used in robots to learn how to walk.

Jin et al. [43] used machine learning methods to predict the onset dose for void swelling (shown in Fig. 5), based on the alloy's chemical composition. Zhang et al. [44] was able to apply machine learning to predict solid solubility based on the Hume-Rothery rules with decent precision. His machine learning algorithm derived similar rules like Hume-Rothery, but slightly different parameters. Jin's and Zhang's works are a vivid example for structure-property linkage in materials informatics.

5.2. Data mining

Data mining is a branch of machine learning, but it has several vague definitions. Some use it as a synonym for knowledge discovery from data (KDD), others see it as an essential step in the process of knowledge discovery. In general, data mining uses mathematical models to find patterns in large datasets. Then, these patterns can be used to detect clusters, associations, or anomalies or they are used to make predictions to new observations. Based on the Cross-Industry Standard Process for Data Mining (CRISP-DM), the data mining workflow can be summarized as depicted in Fig. 18 [34], [45]–[47].

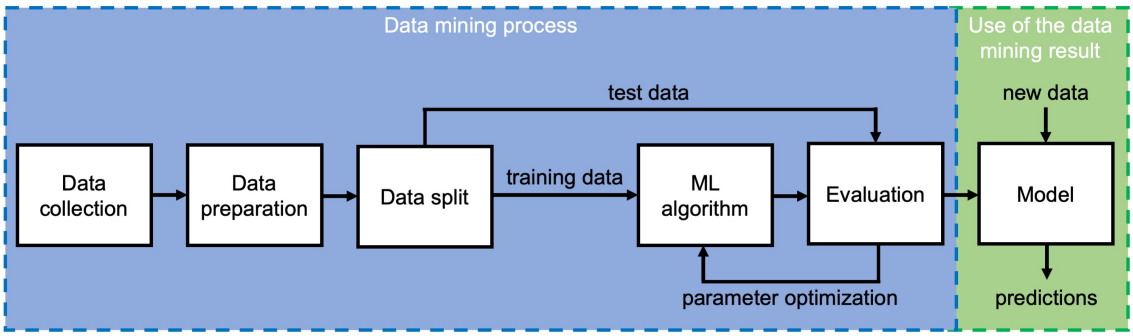

Fig. 18: Schematic workflow in supervised data mining. In the figure, the predictive model as usage of the data mining result is just an example.

Depending on the desired output, meaningful data in sufficient amount has to be collected first. Often, data is collected in a rational database consisting of one or several tables. Normally, each table exhibits a set of attributes as columns and a

large set of observation or measurements as rows. Then, the dataset has to be prepared to clear noisy and inconsistent data and to replace missing values. Especially in supervised learning, some of the observations have to be reserved for the later evaluation. To assess the algorithm's performance independently later, the split is done randomly. The ML method is then trained by the training data only. One can choose from numerous types of ML methods, all having pros and cons in precision, computational speed, and data amount handled. Underlining the importance of choosing the appropriate method, Fig. 19 shows conceptionally how differently patterns can be derived from the same training dataset [45], [47].

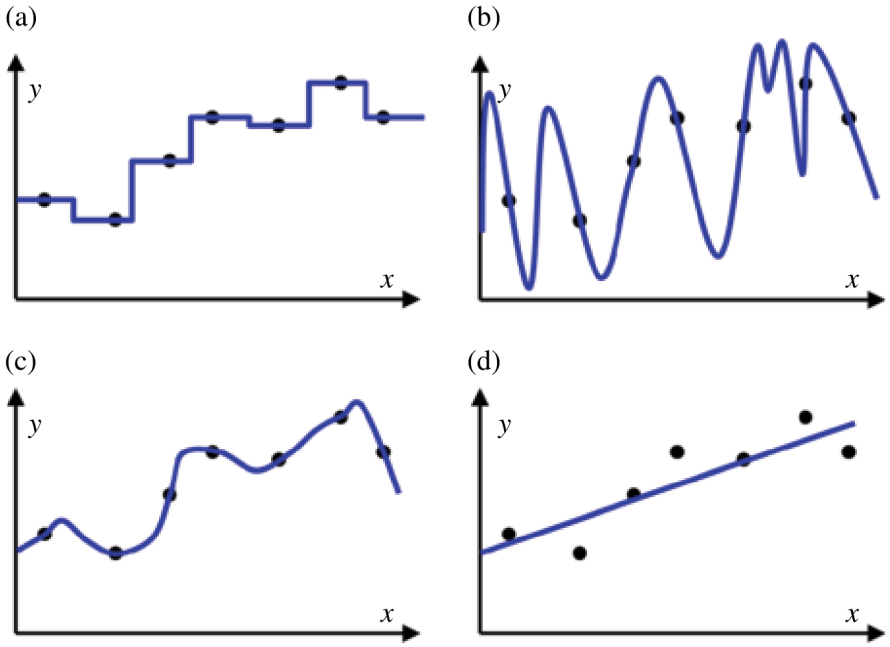

Fig. 19: Four different patterns (a), (b), (c) and (d) derived from the same training data set (black dots) where the x-values represent features and the y-values represent targets [42].

Depending on the ML task, there is a wide range of metrics to evaluate the performance of a trained ML algorithm. In supervised learning, the algorithm can be trailed with the features contained in the test data. Because it is unfamiliar with the test dataset, the algorithm predicts the target values, which one can compare with the known correct targets afterwards. This insight can be used to optimize the algorithm's parameters in an iterative process until the desired accuracy is reached [45].

5.3. Text mining

Like data mining, text mining is also a branch of machine learning and it has a variety of definitions. Similarly, text mining can be seen as a process within KDD or as the extraction of information from written text. Further, text itself can be represented by data and methods of data mining might be applied to find text patterns. This application is often called “text data mining” [48].

This thesis focus on information extraction from written text published in academic articles and papers. Therefore, it is important to understand the two different forms information is provided. Structured data describes the regular and predictable organized form of information, like tables or a set of lists. So, tables link pieces of information together, called “relation”. Formulated sentences adding up to text is unstructured data, like this master thesis containing a lot of information spread over several paragraphs, chapters, and pages. Unstructured data cannot be processed digitally though. Thus, the main goal of information extraction by text mining is to translate unstructured in machine-readable structured data, as summarized in the visual examples in Fig. 20 [49].

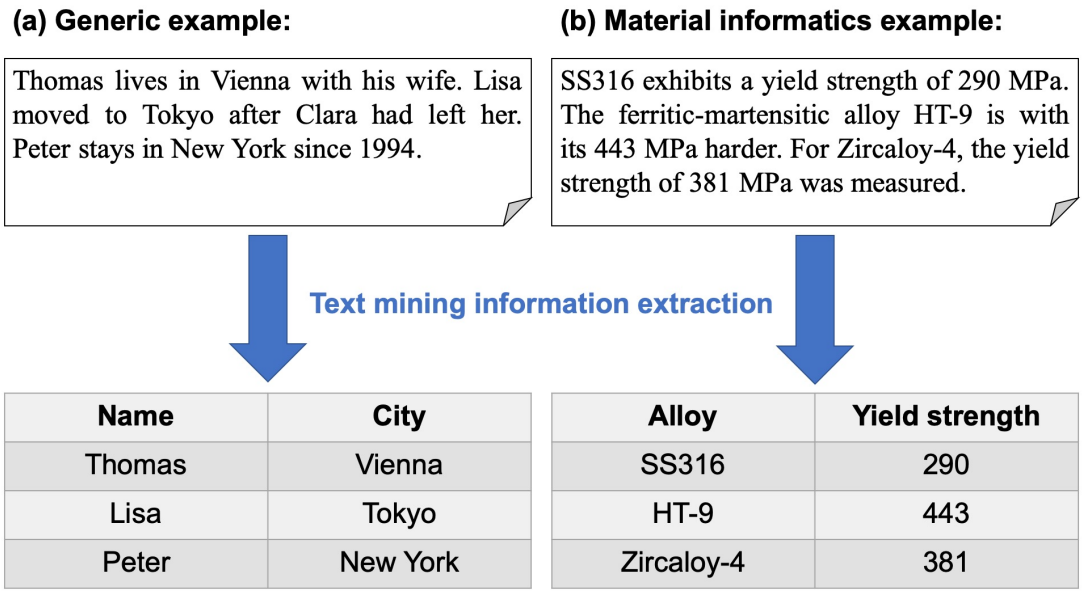

Fig. 20: Two examples **(a)** and **(b)** for information extraction in text mining.

In the generic example of Fig. 20 (a), one is interested in the cities the people live in. So, the information of the people’s names and their localization needs to be retrieved from the text. Along this example, some important aspects of the

workflow of text mining information extraction can be outlined, as depicted in Fig. 21.

To make unstructured text processable for computers, the text has to be broken into its individual sentences. Every sentence becomes an entry in a list. Then the sentences are split into the words they consist of, also called “tokens”. Now, the text is represented as a list of sentences, where every list element is a list of words itself [49].

Every word can be classified in word categories, like nouns, verbs, adjectives, adverbs, etc. This classification step is called “part-of-speech (POS) tagging” and is often done with the help of free available online libraries, dictionaries, and programs. For a computer this step is not trivial, as the word category is determined by context many times. Words like “current”, “list”, or “break” have different meanings and thus can be used as nouns, verbs, or adjectives. Because POS-tagging is a classification task, machine learning methods are applied to identify the correct word category [49].

Depending on the desired output, the information of interest, called “entities”, has to be found. Phrases like “New York” or “yield strength” consist out of two or more words but describe one entity. Their detection can be secured by libraries and dictionaries too [49]. In the example of Fig. 21, all the city names are detected by matching with an online library and all the people’s names are determined as the other output class, e.g. simply by their capital letter.

Finally, the relations described within the sentences have to be recognized as well to distinguish related entities from unrelated ones [49]. Fig. 21 shows that Clara is identified as an entity precisely, because it is a name. However, her name is not incorporated in the database correctly, because of the missing relation to a city.

The example of Fig. 21 also clarifies that the first steps, namely sentence segmentation, tokenization, and POS-tagging, are quite standardized and common in text mining. The logic of entity and relation recognition have to be customized to the information extraction task.

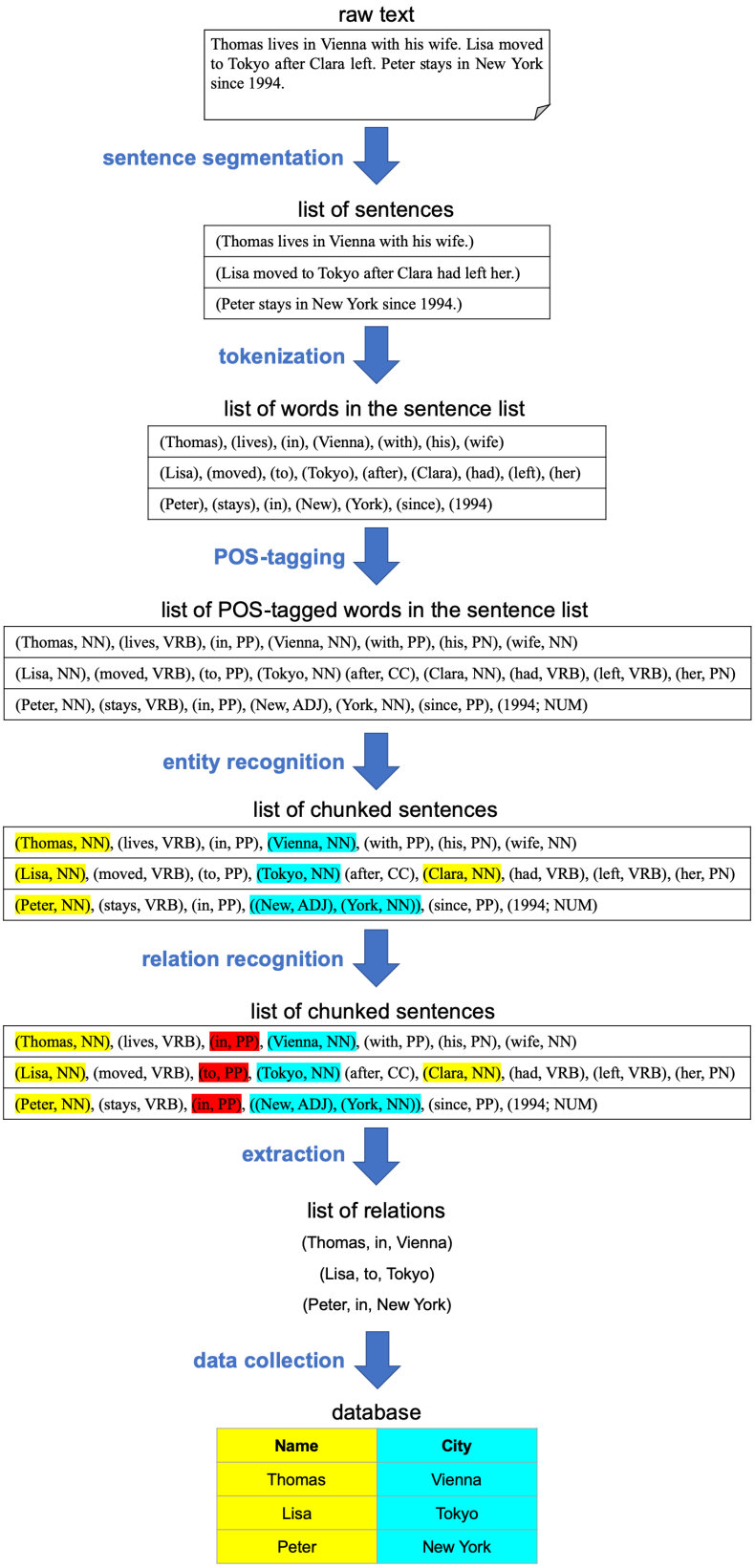

Fig. 21: Exemplary workflow of text mining information extraction (based on [49]).

6. Refrences

[1] M. F. Ashby, *Materials Selection in Mechanical Design Third Edition*, Third Edit. Elsevier Butterworth-Heinemann, 2005.

[2] International Organization on Standardization, *ISO 32000-1: Document management -- Portable document format -- Part 1*. 2008.

[3] T. Allen, J. Busby, M. Meyer, and D. Petti, “Materials challenges for nuclear systems,” *Materials Today*, vol. 13, no. 12, pp. 14–23, 2010, doi: 10.1016/S1369-7021(10)70220-0.

[4] “IAEA Advanced Reactors Information System (ARIS).” [Online]. Available: https://aris.iaea.org. [Accessed: 02-Aug-2019].

[5] Generation IV International Forum (GIF), “Technology Roadmap Update for Generation IV Nuclear Energy Systems,” 2014.

[6] P. Hosemann, D. Frazer, M. Fratoni, A. Bolind, and M. F. Ashby, “Materials selection for nuclear applications: Challenges and opportunities,” *Scripta Materialia*, vol. 143, pp. 181–187, 2018, doi: 10.1016/j.scriptamat.2017.04.027.

[7] C. R. F. Azevedo, “Selection of fuel cladding material for nuclear fission reactors,” *Engineering Failure Analysis*, vol. 18, no. 8, pp. 1943–1962, 2011, doi: 10.1016/j.engfailanal.2011.06.010.

[8] ASTM International, *A 771/A 771M – 95: Standard Specification for Seamless Austenitic and Martensitic Stainless Steel Duct Tubes for Liquid Metal-Cooled Reactor Core Components*. 2001.

[9] ASTM International, *B351/B351M-13: Standard Specification for Hot-Rolled and Cold-Finished Zirconium and Zirconium Alloy Bars, Rod, and Wire for Nuclear Application*. 2018.

[10] R. L. Klueh and A. T. Nelson, “Ferritic/martensitic steels for next-generation reactors,” *Journal of Nuclear Materials*, vol. 371, no. 1–3, pp. 37–52, 2007, doi: 10.1016/j.jnucmat.2007.05.005.

[11] P. Hosemann, S. Kabra, E. Stergar, M. J. Cappillo, and S. A. Maloy, “Micro-structural characterization of laboratory heats of the Ferric/Martensitic steels HT-9 and T91,” *Journal of Nuclear Materials*, vol. 403, no. 1–3, pp. 7–14, 2010, doi: 10.1016/j.jnucmat.2010.05.005.

[12] G. S. Brady, H. H. Clauser, and J. A. Vaccari, “Materials, Their Properties and Uses (U - Z),” in *Materials Handbook: An Encyclopedia for Managers, Technical Professionals, Purchasing and Production Managers,*

Technicians, and Supervisors, 15th ed., New York: McGraw-Hill Education, 2002.

[13] C. L. Withmarsh, “Review of Zircaloy-2 and Zircaloy-4 Properties Relevant to N.S. Savannah Reactor Design,” *UC-80-Reactor Technology, TID-4500 (17th ed.)*, no. Report No. ORNL-3281, p. 70, 1962, doi: Report No. ORNL-3281, UC-80-Reactor Technology, TID-4500 (17th ed.).

[14] G. Kessler, *Sustainable and Safe Nuclear Fission Energy*. Berlin, Heidelberg: Springer Berlin Heidelberg, 2012.

[15] G. S. Was, *Fundamentals of Radiation Materials Science: Metals and Alloys, Second Edition*, Second Edi. New York, NY: Springer New York, 2017.

[16] E. A. Kenik and J. T. Busby, “Radiation-induced degradation of stainless steel light water reactor internals,” *Materials Science and Engineering R: Reports*, vol. 73, no. 7–8, pp. 67–83, 2012, doi: 10.1016/j.mser.2012.05.002.

[17] J. L. Brimhall, H. E. Kissinger, and G. L. Kulcinski, “The Effect of Temperature on Void Formation in irradiated pure and impure metals,” in *Proceedings of radiation-induced voids in metals*, 1972, doi: 10.2172/4694493.

[18] P. J. Maziasz and C. J. McHargue, “Microstructural evolution in annealed austenitic steels during neutron irradiation,” *International Materials Reviews*, vol. 32, no. 1, pp. 190–219, 1987, doi: 10.1179/095066087790150331.

[19] P. J. Maziasz, “Overview of microstructural evolution in neutron-irradiated austenitic stainless steels,” *Journal of Nuclear Materials*, vol. 205, no. C, pp. 118–145, 1993, doi: 10.1016/0022-3115(93)90077-C.

[20] S. J. Zinkle, P. J. Maziasz, and R. E. Stoller, “Dose dependence of the microstructural evolution in neutron-irradiated austenitic stainless steel,” *Journal of Nuclear Materials*, vol. 206, no. 2–3, pp. 266–286, 1993, doi: 10.1016/0022-3115(93)90128-L.

[21] F. A. Garner and D. S. Gelles, “Neutron-Induced Swelling of Commercial Alloys at Very High Exposures,” *Effects of Radiation on Materials: 14th International Sym- posium {Volume II)*, no. May 1990, pp. 673–683, 1990.

[22] Y. Chen, “Irradiation effects of HT-9 martensitic steel,” *Nuclear Engineering and Technology*, vol. 45, no. 3, pp. 311–322, 2013, doi: 10.5516/NET.07.2013.706.

[23] P. G. Shewmon, “Radiation-induced swelling of stainless steel,” *Science*, vol. 173, no. 4001, pp. 987–991, 1971, doi: 10.1126/science.173.4001.987.

[24] G. E. Lucas, “The evolution of mechanical property change in irradiated austenitic stainless steels,” *Journal of Nuclear Materials*, vol. 206, no. 2–3, pp. 287–305, 1993, doi: 10.1016/0022-3115(93)90129-M.

[25] J. T. Busby, M. C. Hash, and G. S. Was, “The relationship between hardness and yield stress in irradiated austenitic and ferritic steels,” *Journal of Nuclear Materials*, vol. 336, no. 2–3, pp. 267–278, 2005, doi: 10.1016/j.jnucmat.2004.09.024.

[26] G. R. Irwin, “Analysis of stresses and strains near the end of a crack transversing a plate,” *Trans. ASME, Ser. E, J. Appl. Mech.*, vol. 24, pp. 361–364, 1957.

[27] J. R. Rice, “A path independent integral and the approximate analysis of strain concentration by notches and cracks,” *Journal of applied mechanics*, vol. 35, no. 2, pp. 379–386, 1968.

[28] A. E. Ismail, A. K. Ariffin, S. Abdullah, and M. Ghazali, “Stress intensity factors for surface cracks in round bar under single and combined loadings,” *Meccanica*, vol. 47, Jun. 2012, doi: 10.1007/s11012-011-9500-7.

[29] ASTM International, *Standard Test Method for Linear-Elastic Plane-Strain Fracture Toughness K_Ic of Metallic Materials*. 2010.

[30] International Atomic Energy Agency (IAEA), “Applicability of the leak before break concept,” 1993.

[31] ASME, “ASME BPVC Section III Division 1, Subsection NB,” *ASME Boiler & Pressure Vessel Code*, 2015, doi: 10.1016/B978-1-4160-4210-5/00021-9.

[32] M. F. Ashby, “A first report on deformation-mechanism maps,” *Acta Metallurgica*, vol. 20, no. 7, pp. 887–897, 1972, doi: 10.1016/0001-6160(72)90082-X.

[33] S. J. Zinkle and G. E. Lucas, “Deformation and fracture mechanisms in irradiated FCC and BCC metals,” *Fusion Materials Semiannual Report for period ending*, pp. 101–125, 2003.

[34] K. Rajan, “Materials informatics,” *Materials Today*, vol. 8, no. 10, pp. 38–45, 2005, doi: 10.1016/S1369-7021(05)71123-8.

[35] R. Ramprasad, R. Batra, G. Pilania, A. Mannodi-Kanakkithodi, and C. Kim, “Machine learning in materials informatics: Recent applications and

prospects," *npj Computational Materials*, vol. 3, no. 1, 2017, doi: 10.1038/s41524-017-0056-5.

[36] J. M. Rickman, T. Lookman, and S. v. Kalinin, "Materials informatics: From the atomic-level to the continuum," *Acta Materialia*, vol. 168, pp. 473–510, 2019, doi: 10.1016/j.actamat.2019.01.051.

[37] G. J. Mulholland and S. P. Paradiso, "Perspective: Materials informatics across the product lifecycle: Selection, manufacturing, and certification," *APL Materials*, vol. 4, no. 5, 2016, doi: 10.1063/1.4945422.

[38] National Research Council, "Materials in the New Millennium: Responding to Society's Needs," in *2000 National Materials Advisory Board Forum*, 2001, p. 54, doi: 10.17226/10187.

[39] J. P. Holdren *et al.*, "Materials Genome Initiative Strategic Plan," 2014.

[40] H. L. Eiselstein and D. J. Tillack, "The Invention and Definition of Alloy 625," in *Superalloys 718, 625 and Various Derivatives (1991)*, 1991, doi: 10.7449/1991/Superalloys_1991_1_14.

[41] A. Géron, *Hands-on machine learning with Scikit-Learn and TensorFlow: concepts, tools, and techniques to build intelligent systems*, 2nd Editio. O'Reilly, 2019.

[42] T. Mueller, A. G. Kusne, and R. Ramprasad, "Machine Learning in Materials Science," in *Reviews in Computational Chemistry*, vol. 29, A. L. Parrill and K. B. Lipkowitz, Eds. New Jersey: John Wiley & Sons, 2016, pp. 186–273.

[43] M. Jin, P. Cao, and M. P. Short, "Predicting the onset of void swelling in irradiated metals with machine learning," *Journal of Nuclear Materials*, vol. 523, pp. 189–197, 2019, doi: 10.1016/j.jnucmat.2019.05.054.

[44] H. Zhang *et al.*, "Application of fuzzy learning in the research of binary alloys: Revisit and validation," *Computational Materials Science*, vol. 172, no. October 2019, p. 109350, 2020, doi: 10.1016/j.commatsci.2019.109350.

[45] F. Provost and T. Fawcett, "Data Science for Business: What You Need to Know About Data Mining and Data-Analytic Thinking," *Sebastopol, Calif. : O'Reilly.* 2013.

[46] C. Shearer, "The CRISP-DM model: The New Blueprint for Data Mining," *Journal of Data Warehousing*, vol. 5, no. 4, pp. 13–22, 2000.

[47] J. Han, M. Kamber, and J. Pei, *Data Mining: Concepts and Techniques*, 3rd Editio. Elsevier, 2012.

[48] A. Hotho, A. Nürnberger, and G. Paaß, “A Brief Survey of Text Mining,” *LDV Forum - GLDV Journal for Computational Linguistics and Language Technology*, 2005, doi: 10.1111/j.1365-2621.1978.tb09773.x.

[49] S. Bird, E. Klein, and E. Loper, *Natural Language Processing with Python: Analyzing Text with the Natural Language Toolkit*. 2009.